Materials Transactions, Vol. 61, No. 4 (2020) pp. 678 to 684

Work-Hardening Mechanism in High-Nitrogen Austenitic Stainless Steel*1

Takuro Masumura[1,*2], Yuki Seto[2,*3], Toshihiro Tsuchiyama[1,3] and Ken Kimura[4]

[1]*Research Center for Steel, Kyushu University, Fukuoka 819-0395, Japan*
[2]*Graduate School of Engineering, Kyushu University, Fukuoka 819-0395, Japan*
[3]*Department of Materials Science and Engineering, Kyushu University, Fukuoka 819-0395, Japan*
[4]*Titanium & Stainless Steel Research Lab., Steel Research Laboratories, NIPPON STEEL CORPORATION, Chiba 293-8511, Japan*

The remarkably high work-hardening rate in high-nitrogen austenitic stainless steels is generally believed to be due to the promotion of dislocation accumulation by nitrogen addition. However, analysis of dislocation accumulation behavior by the modified Williamson-Hall/Warren-Averbach method reveals that no difference to the increment of the dislocation density during deformation exists between austenitic steels with and without nitrogen. Since cross slipping is markedly suppressed in high-nitrogen steels, the moving dislocations are back-stressed by the planar dislocation arrays. This induces the deformation resistance and the high work-hardening rate.
[doi:10.2320/matertrans.H-M2020804]

(Received November 1, 2019; Accepted January 21, 2020; Published March 25, 2020)

Keywords: *austenitic stainless steel, dislocation density, planar dislocation array, nitrogen, mWH/WA method*

1. Introduction

Nitrogen (N), one of the alloying elements for steel, is used with the aim of improving the material's corrosion resistance,[1)] austenitic stability,[2–5)] and its mechanical strength. In austenitic stainless steel with low yield stress, N is recognized as an effective alloying element for solid solution strengthening[6–9)] and increasing the work-hardening rate.[9–13)] However, the mechanism for this strengthening by N has been unclear. Though some researchers have explained that I-S (interstitial-substitutional) pairs or short-range order (SRO),[14–16)] which consisted of substitutional elements, such as Cr and Mo, and the interstitial element, N, could cause the high yield stress in high-N austenites, no one has confirmed their atomic arrangement and structure.

The work-hardening behavior has been discussed in terms of the unique dislocation arrangement developed in high-N austenitic steel. In high-N steels, it is well known that dislocations are aligned on the same slip plane, because cross slipping is remarkably suppressed.[10,12,17)] Such a dislocation structure is called a planar dislocation array. The reason why planar dislocation array develops is not clear but is generally explained by the presence of SRO. The SRO is thought to effectively behave as a barrier to dislocation movement, but once the SRO is cut by dislocation passage, subsequent dislocation can easily move and is concentrated on the specific slip system, which results in the planar dislocation arrangement.[18)] Kubota *et al.*[10)] observed the Lomer-Cottrell sessile dislocation formed by crossing of planar dislocations and suggested that increases of the sessile dislocations during deformation increases the work-hardening rate because the sessile dislocation act as the barrier to dislocation movement. In addition, suppression of the cross slipping and formation of the sessile dislocations is considered effective for promotion of dislocation accumulation, and thus dislocation density in deformed high-N austenites is expected to be high.[10–12)]

However, no prior research has quantitatively evaluated dislocation density of high-N austenitic steel. This is because it was difficult to estimate dislocation density in austenitic stainless steels. Direct observation using TEM is one of the methods capable of measuring dislocation density, but it is extremely difficult to identify each dislocation and to count them all in a strained austenite where dislocation density can be over $10^{15}\,m^{-2}$. Therefore, the Williamson-Hall (WH) method,[19)] which estimates the dislocation density from the full-width at half-maximum (FWHM) and diffraction angle of X-ray diffraction (XRD) peaks, has often been applied. Micro strain (ε) obtained by the WH method can be easily converted to dislocation density: for example, $\rho = 9.3 \times (\varepsilon/b)^2$ in ferritic steels[20)] (ρ: dislocation density [m^{-2}], b: magnitude of the Burgers vector [m]). This method is applicable only when there are some diffraction planes with low elastic anisotropy, such as in ferritic steels. However, it is difficult to evaluate dislocation density when the elastic modulus of each diffraction plane is significantly different, such as in austenitic stainless steel with FCC structure, because ε cannot be calculated accurately. On the other hand, the modified Williamson-Hall/Warren-Averbach (mWH/WA) method[21)] was recently proposed, including a contrast factor (the correction parameter for the elastic anisotropy in each diffraction plane). This method enables the exact evaluation of the dislocation density for metallic materials with large elastic anisotropy, like austenitic stainless steels. Although the mWH/WA method is more complicated than the WH method, the mWH/WA method is very useful to discuss the relationship between dislocation structure and the dislocation strengthening mechanism in metallic materials because it can quantitatively evaluate not only dislocation density but also dislocation characterization and arrangement. In addition, a direct observation of dislocation distribution and stress field generated by dislocation using SEM, TEM and the EBSD-Wilkinson method[22,23)] would also informative to understand the work-hardening mechanism in high-N austenitic stainless steels.

*1This Paper was Originally Published in Japanese in J. Jpn. Soc. Heat Treat. **59** (2019) 222–229. In this article, we have used the expressions of 'High-N steel' and 'Low-N steel' instead of 'High N steel' and 'Low N steel' in the original Japanese article.

*2Corresponding author, E-mail: masumura@zaiko.kyushu-u.ac.jp
*3Graduate Student, Kyushu University

In this study, appropriately 0.5 mass% N was added to stable austenitic stainless steel, type 316L, by solution nitriding method, and the dislocation density and arrangement in the deformed specimens were quantitatively evaluated by the mWH/WA method. In addition, EBSD-Wilkinson measurements revealed the relationship between dislocation structure and local strain in austenite grains. We then discussed the effect of N on work-hardening behavior in austenitic stainless steels.

2. Experimental Procedure

Commercially available stable austenitic stainless steel, type 316L (Fe–17.6Cr–12.3Ni–1.19Mn–0.55Si–2.08Mo–0.012C–0.04N [mass%] alloy), was used in this study. The plate specimens were cut with 2 mm thickness and subjected to the following two types of heat treatments. Some specimens were solution-treated at 1473 K in an Ar atmosphere of 0.1 MPa for 20 h, followed by water cooling (low-N steel). Solution-nitriding[8] was applied to other specimens at 1473 K in an N_2 atmosphere of 0.1 MPa for 20 h, followed by water cooling (high-N steel). The chemical composition of Ar gas was Ar > 99.999%, O_2 < 2 ppm, N_2 < 10 ppm, CO < 0.5 ppm, CO_2 < 0.5 ppm, CH_4 < 0.5 ppm and H_2O < 5 ppm, and that of N_2 gas is N_2 > 99.999%, O_2 < 2 ppm, CO < 1 ppm, CO_2 < 1 ppm, CH_4 < 1 ppm and H_2O < 5 ppm. These gases were purified by a gas column (GC-RX, Nikka Seiko, O_2 < 0.002 ppm) and a dry column (DC-SXC, Nikka Seiko). The average N concentration in high-N steel measured with a Nitrogen/Oxygen Combustion Analyzer (EMGA-620W, HORIBA) was 0.45 mass% N, which is similar to an equilibrium concentration (0.49 mass% N[8]) predicted by a thermodynamics calculation. To confirm the uniform N solution in plate specimen, the hardness distribution from the sample surface to the inside is presented in Fig. 1. In high-N steel, the hardness was remarkably increased by solid solution strengthening of N and was almost the same value everywhere, which means that N has uniformly distributed in the specimen.

Tensile testing was conducted at ambient temperature at an initial strain rate of $1 \times 10^{-3}\,s^{-1}$, for the plate specimens with gauge dimensions of $25 \times 10 \times 2$ mm (length × width × thickness). In some samples, tensile testing was interrupted at several strains within uniform deformation range. The microstructures of the specimens were observed by field-emission scanning electron microscopy (FE-SEM: SIGMA500, Zeiss) and transmission electron microscopy (TEM: JEM-2100HC (at The Ultramicroscopy Research Center, Kyushu University), JEOL). As for SEM observations, electron-channeling contrast imaging (ECCI) was carried out by using a backscattered-electron detector operating at an accelerating voltage 20 kV and a working distance of 4.5 mm. The crystallographic orientation was mapped by means of the electron backscatter diffraction (EBSD) method using an FE-SEM. Operated at an accelerating voltage 20 kV with a step size of 1.5 μm, the data obtained by EBSD were analyzed using software programs for automatic crystal orientation mapping (OIM analysis, TSL). Additionally, microscopic distribution of the elastic strain was visualized by the EBSD/Wilkinson method.[22,23] *In-situ* observation during tensile testing within the SEM was performed for smaller plate specimens with gauge dimensions of $10 \times 2 \times 1$ mm (length × width × thickness). The obtained EBSD patterns were analyzed using dedicated software (Cross Court 3.0) for mapping the elastic strain. (The measurement conditions were an accelerating voltage 20 kV, a step size of 1 μm, 1×1 pixel binning, and 100 ms exposure.) The reference point for the strain analysis was obtained from the solution-treated specimen without distortion.

X-ray line profile analysis was performed to examine dislocation density and dislocation characterization. The tensile-tested specimens with different strain were polished with sand paper and then electropolished in an acid mixture (H_3PO_4:CrO_3 = 2:1) by more than 50 μm, in order to eliminate the effect of strained layers by grinding.[24] The X-ray diffraction measurements, with a Cu-Kα_1 radiation source (wavelength: 0.15418 nm), were carried out at 40 kV and 40 mA. The rotation speed of the detector was 0.8°/min. Since obtained X-ray line profiles include the instrumental function, the effect was corrected based on Voigt profile analysis,[25] using the standard materials with quite low dislocation density (type 316L solution-treated at 1473 K for 3 h, followed by furnace cooling).

The mWH method[21] proposed by Ungár *et al.* is defined as follows:

$$\Delta K = \frac{0.9}{D} + \sqrt{\frac{\pi A^2 b^2 \rho}{2}} K\sqrt{C} + O(K^2C) \qquad (2.1)$$

where $K = 2\sin\theta/\lambda$ and $\Delta K = 2\beta\cos\theta/\lambda$ (λ: wavelength of X-ray, θ: diffraction angle [rad.] and β: FWHM of diffraction peak [rad]). In addition, D, A, O and C denote the crystallite size, a parameter depending on the effective outer cutoff radius of dislocation, higher-order term of $K\sqrt{C}$, and the average contrast factor, respectively. The above equation, including C, considers the elastic anisotropy in a WH plot. C, obtained by the mWH method, is used in the mWA method to estimate the dislocation density. The equations for the mWA method are defined as follows:[21]

$$\ln A(L) \cong \ln A^S(L) - Y(L)(K^2C) + Q(K^4C^2) \qquad (2.2)$$

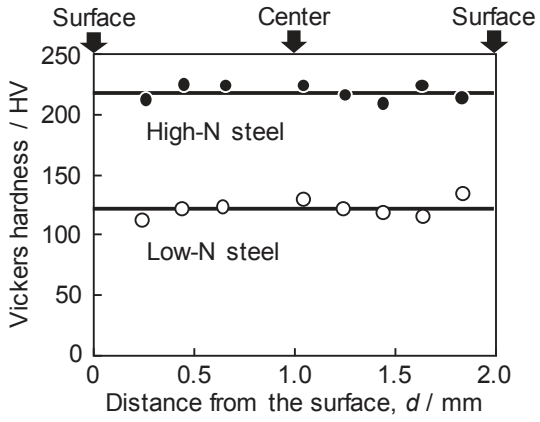

Fig. 1 Distribution of Vickers hardness in the thickness direction of high- and low-N steel plate specimens.

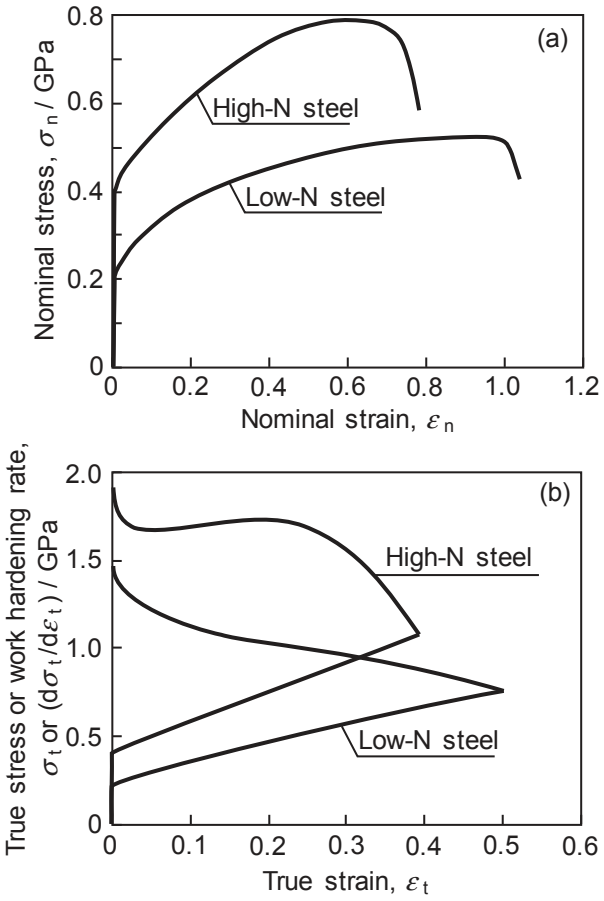

Fig. 2 (a) Nominal stress-strain curves and (b) changes in true stress and work-hardening rate as a function of the true strain in high- and low-N steels.

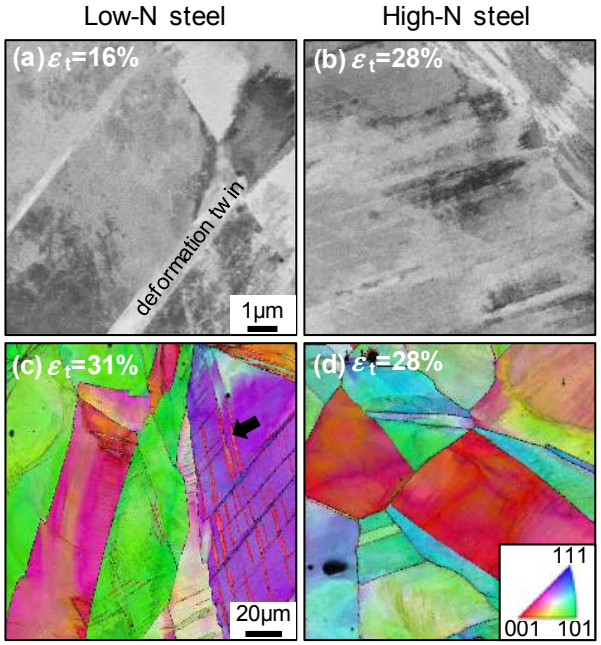

Fig. 3 (a), (b) ECC images and (c), (d) crystallographic orientation maps of tensile-deformed (a), (c) low-N, and (b), (d) high-N steels.

$$Y(L) = \rho \frac{\pi b^2}{2} L^2 \ln\left(\frac{R_e}{L}\right) \tag{2.3}$$

where L, $A(L)$, $A^S(L)$, Re and Q represent the Fourier variable, the real part of the Fourier coefficient, the size Fourier coefficient, the effective outer cutoff radius of dislocation, and a coefficient for the higher-order term of K^2C, respectively. The detailed analysis procedure is described in the references.[21,26–28] As a result, dislocation density ρ and Re in eq. (2.3) can be calculated by the mWH/WA method.

3. Results and Discussion

3.1 Effect of nitrogen on mechanical properties and deformation microstructure

Figure 2 shows the nominal stress-strain curves (Fig. 2(a)) and the changes in true stress and work-hardening rate as a function of true strain (Fig. 2(b)) in high- and low-N steels. The yield stress of high-N steel is approximately twice as high as that of low-N steel due to the solid solution strengthening by N, and furthermore, high tensile strength of about 800 MPa was obtained without a lack of elongation. In addition, the work-hardening rate in high-N steel is remarkably higher at any strain region, which means that N improves the work hardenability of austenite. Figure 3 shows the ECCI (Fig. 3(a), (b)) and crystallographic orientation maps (Fig. 3(c), (d)) of tensile-deformed low-N (3(a), (c)) and high-N (3(b), (d)) steels. From ECCI, in which the elastic strain field owing to dislocation can be observed as the white contrast, it is found that dislocations in high-N steel (Fig. 3(b)) are linearly arrayed, in comparison to those in low-N steel (Fig. 3(a)). In other words, the planar dislocation arrays form because the cross slipping of dislocation is suppressed in high-N steel. Moreover, crystal orientation maps reveal that there are many deformation twins (indicated by an array in Fig. 3(c)) having a misorientation of 60° around the ⟨111⟩ common rotation axis against the austenite matrix in low-N steel, while such a structure is hardly observed in high-N steel (Fig. 3(d)). It is generally known that deformation twins easily form in austenite, with its lower stacking-fault energy,[29] indicating that the reason why deformation twinning is suppressed in high-N steel is that N increases the stacking-fault energy of austenite.[2,3,30] In order to confirm the difference of the dislocation arrangement, the microstructure in both steels given 2% true strain was examined by TEM, as shown in Fig. 4. The dislocation array corresponding to the primary slip can be observed in both steels. The dislocation in low-N steel (Fig. 4(a)) is partially bent and tangled with itself, and then the dislocation cell structure begins to be formed by the cross slipping (indicated by an array arrow in Fig. 4(a)). In comparison, in high-N steel (Fig. 4(b)), a typical planar dislocation array aligned on a straight line is formed and there is no trace of cross slipping. Such a variation of dislocation characteristics by addition of N has been considered to stimulate the dislocation accumulation in high-N steel.

3.2 Effect of nitrogen on dislocation density and dislocation characteristics

In order to confirm whether there is a difference in dislocation density between low- and high-N steels, XRD analysis was conducted for the tensile-deformed specimens. Figure 5 shows the changes in FWHM of $(111)_\gamma$, $(200)_\gamma$,

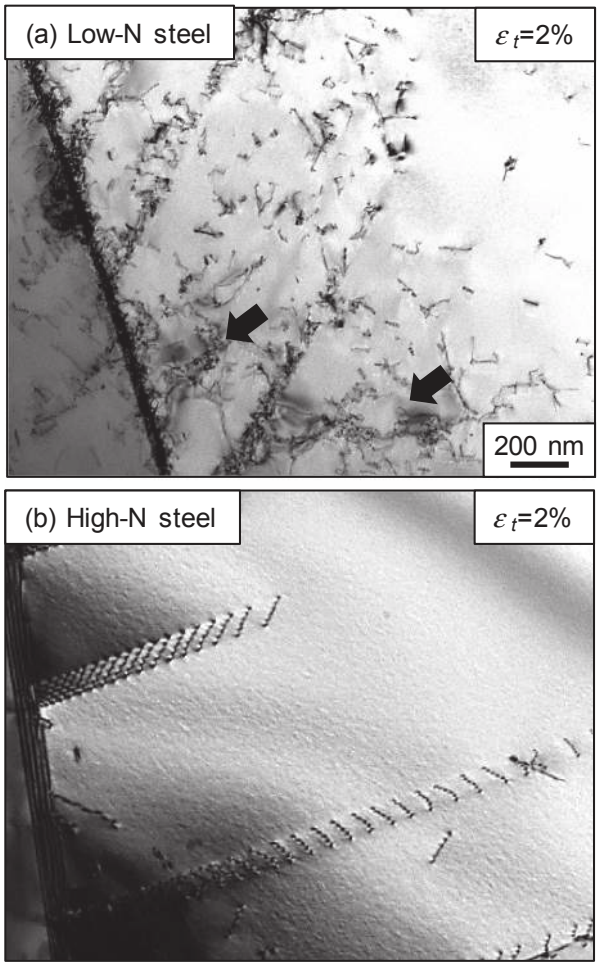

Fig. 4 TEM images of (a) low-N and (b) high-N steels tensile-deformed at 2% true strain.

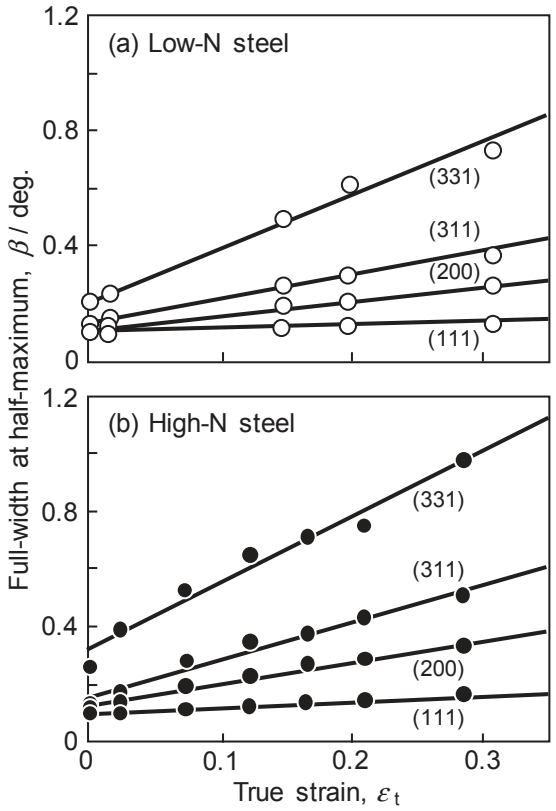

Fig. 5 Changes in full width at half-maximum of $(111)_\gamma$, $(200)_\gamma$, $(311)_\gamma$ and $(331)_\gamma$ peaks as a function of true strain in tensile-deformed (a) low-N and (b) high-N steels.

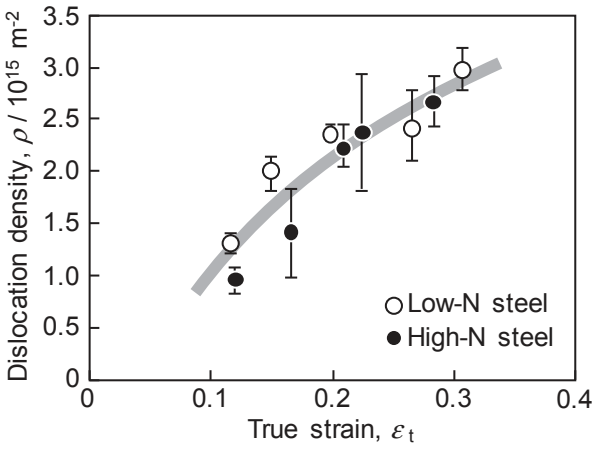

Fig. 6 Changes in dislocation density estimated by mWH/WA method as a function of true strain in low-N and high-N steels.

$(311)_\gamma$ and $(331)_\gamma$ peaks as a function of the true strain in tensile-deformed low-N (Fig. 5(a)) and high-N (Fig. 5(b)) steels. The FWHM of all peaks increased during deformation, and the spread of the FWHM in high-N steel is more remarkable than that in low-N steel, which generally indicates the dislocation density in high-N steel is higher than that in low-N steel. However, the shape of the diffraction peak depends not only on dislocation density, but also on dislocation arrangement, strain field of dislocation and so on. Therefore, analysis for the whole line profile is required to estimate dislocation density. Figure 6 shows the changes in dislocation density calculated by X-ray line profile analysis (mWH/WA method) as a function of true strain in both steels. There was little difference in the increment tendency of dislocation density during deformation, which means the effect of N on the dislocation accumulation behavior was minimal. This result is not consistent with the previous opinion that a high work-hardening rate in high-N steel is caused by dislocation accumulation, so other work-hardening mechanism should be considered.

Other important factor to consider is the dislocation arrangement parameter (M value) obtained by mWH/WA method. When the M value is small, the strain field of each dislocation is small and a stable dislocation structure, such as a dislocation cell, is formed.[31] The M value is a dimensionless parameter expressed by the following equation:

$$M = R_e \times \sqrt{\rho} \tag{3.1}$$

Figure 7 shows the changes in the M value for both specimens as a function of true strain. In low-N steel, the M value is low at the early deformation stage, and hardly changes during further deformation. In comparison, in high-N steel, the M value is close to 1, which means dislocations are randomly distributed at the early deformation stage, and they tend to decrease during deformation. These results indicate that a dislocation cell structure is already formed by cross slipping from the early deformation stage in low-N steel. In comparison, in high-N steel, it is assumed that the elastic strain field of one dislocation increases by repulsion between

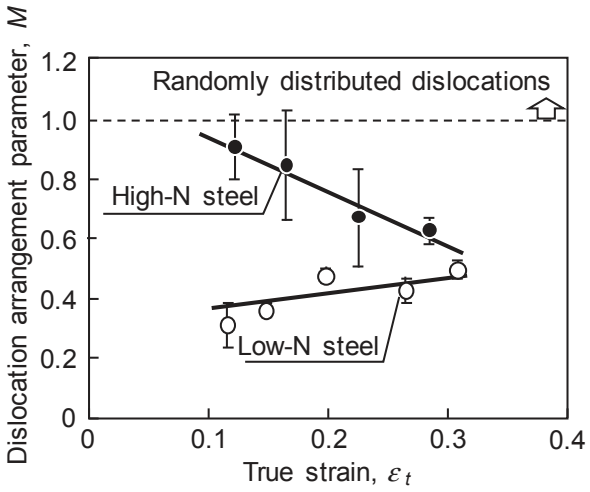

Fig. 7 Changes in dislocation arrangement parameter as a function of true strain in low-N and high-N steels.

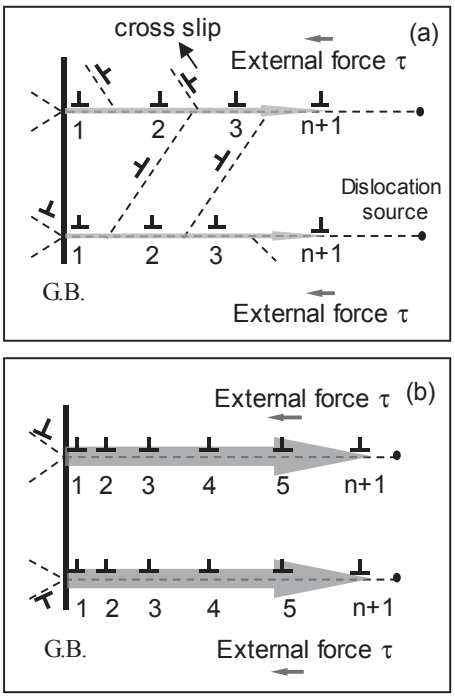

Fig. 8 Schematic illustration showing dislocation pile-up in (a) low-N and (b) high-N steels.

dislocations because planar dislocations are localized on the same slip plane. The above results reveal that the large FWHM in high-N steel is not due to the higher dislocation density, but arises from the difference in dislocation arrangement and strain field of dislocation.

3.3 Work-hardening mechanism in high-nitrogen austenitic steel

When discussing the work-hardening mechanism of metallic materials, the Bailey-Hirsch relationship,[32] which states that the flow stress is proportional to the square root of dislocation density, is often used. However, in this study, the addition of N does not promote dislocation accumulation, which clearly indicates the work-hardening behavior in high-N steel cannot be discussed by only considering the dislocation density. Furthermore, the Bailey-Hirsch relationship is inadequate for the discussion of work-hardening behavior in specimens where dislocations are distributed like in high-N steel, because this relation has been established based on the forest dislocation model[33–35] that dislocations exist uniformly. Therefore, we discuss the work-hardening behavior on high-N steel based on the long-range stress field theory, which is another dislocation strengthening theory.

The planar dislocation in high-N steel forms due to the concentration of dislocation movement on the same slip system, and the movement of the leading dislocation is stopped by obstacles such as a grain boundary or Lomer-Cottrell sessile dislocations, resulting in a pile-up of subsequent dislocations on the same slip plane. Figure 8 presents a schematic illustration showing a pile-up of dislocations in low-N and high-N steels.

Dislocations on the same slip plane (on the arrow in Fig. 8) repel each other because they have the same Burgers vector. The repulsive force f between the two edge dislocations is expressed by the following equation:[36]

$$f = \frac{Gb^2}{2\pi(1-\nu)} \cdot \frac{1}{X} \tag{3.2}$$

where ν, G and X represent Poisson's ratio, the shear modulus and the distance between two dislocations, respectively. When another dislocation approaches from the dislocation source to the pile-up dislocation array, the dislocation is subjected to a back stress in the opposite direction from the stress field formed by the dislocation array, which is a long-range stress field. It can be quantitatively expressed as following equation (3.3), by considering that the back stress due to n pile-up dislocations and the external force τ are balanced.

$$\frac{Gb^2}{2\pi(1-\nu)} \sum_{i=1}^{n-1} \frac{1}{X_i - X_n} = \tau b \tag{3.3}$$

The above equation means that the external force τ required for balancing increases with the increasing number of dislocations (n) on the same slip plane. In order to continue the plastic deformation, it is necessary to introduce (n + 1), the new dislocation, so that the necessary external force τ increases accordingly. The increase in external stress corresponds to the work-hardening. In low-N steel where cross slipping easily occurs, stress relaxation can occur by reducing the number of pile-up dislocations, whereas in high-N steel where cross slipping is rare, the number of pile-up dislocations on the same slip plane significantly increases with deformation, resulting in high work-hardening.

If the long-range stress field actually occurs due to the pile-up of dislocations, a large shear stress should occur at a region closer to the grain boundary affected by pile-up dislocations. In order to verify the long-range stress field, we attempted to observe it by elastic strain analysis in the local region using the EBSD-Wilkinson method. In this study, changes in the distribution of elastic strain were investigated by *in-situ* observation for the same austenite grain under stress in the specimens before tensile testing, just after yielding, and tensile-strained at 5%. Figure 9 shows the crystallographic orientation maps in low-N (Fig. 9(a)) and

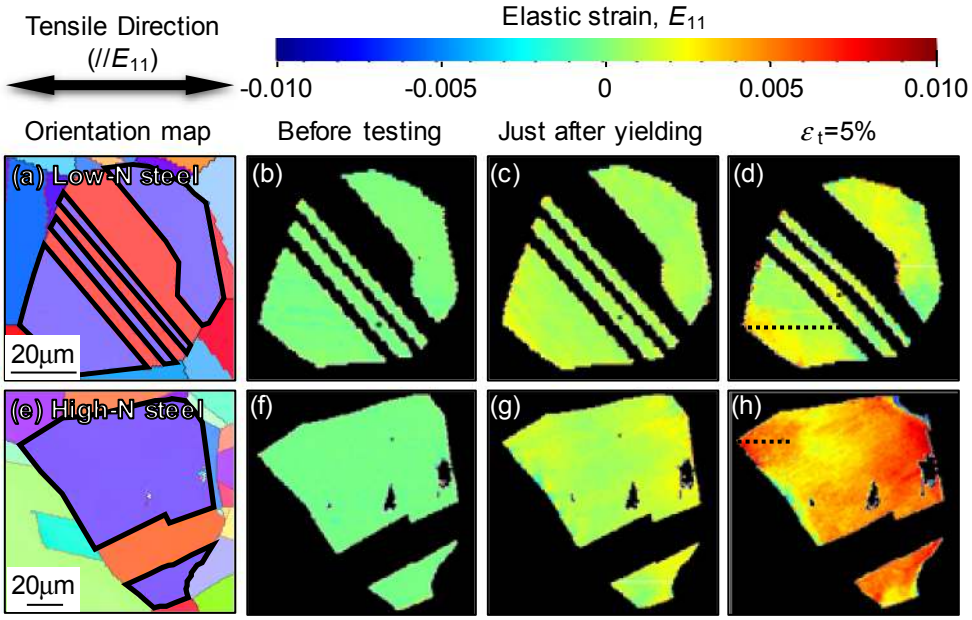

Fig. 9 Crystallographic orientation maps in (a) low-N and (e) high-N steels, and elastic strain (E_{11}) maps in (b)–(d) low-N and (f)–(h) high-N steels, (b), (f) before testing, (c), (g) just after yielding, and (d), (h) strained at $\varepsilon_t = 5\%$.

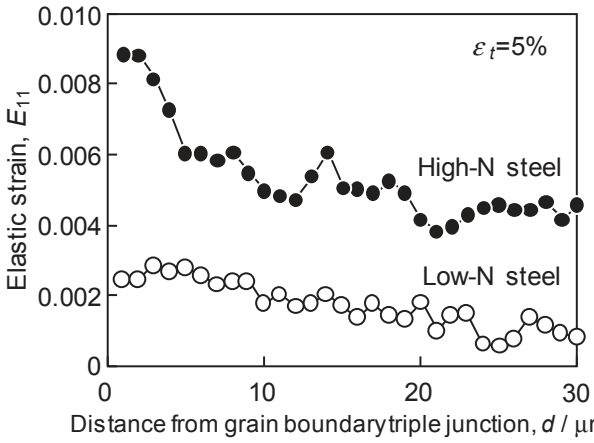

Fig. 10 Changes in elastic strain E_{11} as a function of distance from grain boundary triple junction along the dot line shown in Fig. 9(d) and 9(h).

high-N (Fig. 9(b)) steels before tensile testing. In these maps, the crystal orientation with respect to the tensile direction is shown. The elastic strain analysis was performed on the grains surrounded by the black lines with the same tensile direction ⟨457⟩. Figures 9(b)–(d) and 9(f)–(h) show the elastic strain maps (E_{11}: elastic strain against the tensile direction) in low-N (Fig. 9(b)–(d)) and high-N (Fig. 9(f)–(h)) steels before testing (9(b), (f)), just after yielding (9(c), (g)), and strained at $\varepsilon_t = 5\%$ (9(d), (h)). In both specimens, the elastic strain field in the grains increases with increasing tensile strain. Comparisons between both specimens reveal that there is little effect of N on the distribution of the elastic strain before tensile testing or just after yielding. However, the specimens tensile strained at 5% where work-hardening has occurred, high elastic strain is generated in the high-N steel. As an example of the strain distribution, Fig. 10 presents the changes in elastic strain E_{11} along the dotted line shown in Fig. 9(d) and 9(h) as a function of distance from the grain boundary triple junction, where a large strain concentration was observed in both specimens strained at 5%. In low-N steel, the elastic strain gradually increases as the distance from the grain boundary decreases, whereas in high-N steel, the elastic strain is globally high. This is thought to be because the flow stress applied in high-N steel is about twice that in low-N steel. On the other hand, focusing on the gradient of the elastic strain, the gradient is almost same between both specimens in the region 10 μm or more away from the grain boundary, while the elastic strain rapidly increases within 10 μm from the grain boundary in high-N steel. That is, the stress concentration was caused by the pile-up of many dislocations near the grain boundary in high-N steel, indicating the existence of the long-range stress field that gives large back stress to subsequent dislocations. In conclusion, the increase in deformation resistance due to the long-range stress field is the main factor contributing to the large work-hardening of high-N steel.

In this study, quantitative discussions related to the work-hardening rate are still insufficient, so future research should aim to quantitatively evaluate the planar dislocation structure and develop the theoretical understanding of the work-hardening rate. For this purpose, microstructural analyses, such as line profile analysis, high-resolution SEM, and TEM are expected to play an important role. We should discuss work-hardening while comprehensively considering not only dislocation density but also dislocation arrangement, the difference in properties among grains,[37] and the ratio of edge and screw dislocations.

4. Conclusions

For type 316L steel, a large amount of N was added by the solution nitriding method in order to study the work-hardening mechanism in high-N austenitic stainless steel. This was carried out by examining the dislocation density and distribution by the modified Williamson-Hall/Warren-Averbach method and the local elastic strain mapped by the

EBSD-Wilkinson method for low-N and high-N steels. The obtained results are summarized as follows:

(1) The mechanical properties of high-N steel (0.45 mass% N) are characterized by high yield stress due to the solid solution strengthening of N and high tensile strength due to the increased work-hardening rate. As for the microstructure, planar dislocation arrays formed by suppressing the cross slipping of dislocations are developed in high-N steel.

(2) Dislocation accumulation behavior during tensile deformation in high-N steel is identical to that in low-N steel. Therefore, the high work-hardening rate in high-N steel cannot be explained by the stimulation of dislocation accumulation, so the work-hardening mechanism should be closely related to the development of the planar dislocation array.

(3) In low-N steel, the dislocation arrangement parameter, M, is low from an initial stage of deformation and hardly changes by further deformation, corresponding to the well-developed dislocation cell structure formed by easily causing cross slipping of dislocations. On the other hand, M in high-N steel is higher, which means the elastic strain field of dislocation tends to be large. This corresponds to the large repulsive force between dislocations due to the planar dislocation arrays where dislocations are localized on the same slip plane.

(4) In high-N steel, a large elastic strain gradient is generated at the vicinity of grain boundaries by tensile deformation. This suggests that long-range stress fields arise from planar dislocation causing stress concentrations at grain boundaries and simultaneously gives a large back stress to the following dislocations. The back stress enhances the deformation resistance of the materials, leading to the increase of the work-hardening rate in high-N steel.

Acknowledgements

This work was supported by JSPS KAKENHI Grant Number JP18K14016. We would like to thank Prof. Sigeo Sato (Ibaraki University), Prof. Emeritus Setsuo Takaki and Dr. Daichi Akama (Kyushu University) for their advice on X-ray line profile analysis.

REFERENCES

1) S. Azuma, H. Miyuki and T. Kudo: ISIJ Int. **36** (1996) 793–798.
2) T. Masumura, T. Tsuchiyama, S. Takaki, T. Koyano and K. Adachi: Scr. Mater. **154** (2018) 8–11.
3) T. Masumura, N. Nakada, T. Tsuchiyama, S. Takaki, T. Koyano and K. Adachi: Acta Mater. **84** (2015) 330–338.
4) G.H. Eichelman and F.C. Hull: Trans. Am. Soc. Met. **45** (1953) 77–104.
5) K. Nohara, H. Ono and N. Ohashi: Tetsu-to-Hagané **63** (1977) 772–782.
6) K.J. Irvine, D.T. Llewellyn and F.B. Pickering: J. Iron Steel Inst. **199** (1961) 153–175.
7) T. Tsuchiyama and S. Takaki: Denki-seiko **77** (2006) 163–169.
8) T. Tsuchiyama, H. Ito, K. Kataoka and S. Takaki: Metall. Mater. Trans. A **34** (2003) 2591–2599.
9) K. Tsuboi, T. Tsuchiyama, S. Takaki and S. Tsutsumi: ISIJ Int. **52** (2012) 1872–1878.
10) S. Kubota, Y. Xia and Y. Tomota: ISIJ Int. **38** (1998) 474–481.
11) M. Yoshitake, T. Tsuchiyama and S. Takaki: Tetsu-to-Hagané **98** (2012) 223–228.
12) M. Ojima, Y. Adachi, Y. Tomota, K. Ikeda, T. Kamiyama and Y. Katada: Mater. Sci. Eng. A **527** (2009) 16–24.
13) K. Ikeda, Y. Tomota, J. Suzuki, A. Moriai and T. Kamiyama: Tetsu-to-Hagané **91** (2005) 822–827.
14) A.L. Sozinov and V.G. Gavriljuk: Scr. Mater. **41** (1999) 679–683.
15) M. Murayama, K. Hono, H. Hirukawa, T. Ohmura and S. Matsuoka: Scr. Mater. **41** (1999) 467–473.
16) M. Grujicic, X.W. Zhou and W.S. Owen: Mater. Sci. Eng. A **169** (1993) 103–110.
17) I. Karaman, H. Sehitoglu, H.J. Maier and Y.I. Chumlyakov: Acta Mater. **49** (2001) 3919–3933.
18) X.W. Zhou and M. Grujicic: Calphad **20** (1996) 257–272.
19) G.K. Williamson and W.H. Hall: Acta Metall. **1** (1953) 22–31.
20) D. Akama, T. Tsuchiyama and S. Takaki: J. Soc. Mater. Sci. Jpn. **66** (2017) 522–527.
21) T. Ungár and A. Borbély: Appl. Phys. Lett. **69** (1996) 3173–3175.
22) A.J. Wilkinson: Ultramicroscopy **62** (1996) 237–247.
23) A.J. Wilkinson, G. Meaden and D.J. Dingley: Ultramicroscopy **106** (2006) 307–313.
24) F. Jiang, K. Hirata, T. Masumura, T. Tsuchiyama and S. Takaki: ISIJ Int. **58** (2018) 376–378.
25) T.H.D. Keijser, J.I. Langford, E.J. Mittemeijer and A.B.P. Vogels: J. Appl. Cryst. **15** (1982) 308–314.
26) S. Sato, K. Wagatsuma, M. Ishikuro, E.-P. Kwon, H. Tashiro and S. Suzuki: ISIJ Int. **53** (2013) 673–679.
27) S. Takaki, T. Masumura, F. Jiang and T. Tsuchiyama: Tetsu-to-Hagané **104** (2018) 683–688.
28) T. Masumura, S. Takaki and T. Tsuchiyama: Tetsu-to-Hagané **104** (2018) 717–719.
29) L. Remy and A. Pineau: Mater. Sci. Eng. **28** (1977) 99–107.
30) M. Ojima, Y. Adachi, Y. Tomota, Y. Katada, Y. Kaneko, K. Kuroda and H. Saka: Steel Res. Int. **80** (2009) 477–481.
31) M. Wilkens: Phys. Status Solidi A **2** (1970) 359–370.
32) J.E. Bailey and P.B. Hirsch: Philos. Mag. **5** (1960) 485–497.
33) G. Saada: Acta Metall. **8** (1960) 841–847.
34) F.R.N. Nabarro, Z.S. Basinski and D.B. Holt: Adv. Phys. **13** (1964) 193–323.
35) P.B. Hirsch and T.E. Mitchell: Can. J. Phys. **45** (1967) 663–706.
36) M. Kato: *Introduction to the theory of dislocations*, (Shokabo, Tokyo, 1999) p. 73.
37) Y. Tomota, M. Ojima, S. Harjo, W. Gong, S. Sato and T. Ungár: Mater. Sci. Eng. A **743** (2019) 32–39.